

Mixing in Unstable Shear Flows with Strong Magnetic Fields and High Resistivity

IMOGEN CRESSWELL¹ AND ADRIAN E FRASER²

¹*University of Colorado, Boulder*

²*University of California, Santa Cruz*

ABSTRACT

Turbulence driven by unstable shear flows is an important process in many astrophysical systems. Several instabilities are known to produce shear flows that are unstable to secondary “parasitic” instabilities, for example the fingering instability active in double-diffusively-unstable stellar radiation zones. Whilst most astrophysical flows have extremely high Reynolds and magnetic Reynolds numbers, these parasitic instabilities can occur on much smaller scales, where the effects of viscosity and resistivity are more significant. In the context of the Kelvin-Helmholtz (KH) instability in MHD, this regime is under-explored relative to the high-Rm counterpart. Here we present a systemic parameter study of the Kelvin-Helmholtz (KH) instability in a shear flow with an initially uniform magnetic field in the direction of flow. We use the pseudospectral code Dedalus to solve the 2D incompressible MHD equations with finite resistivity and viscosity with the shear flow maintained by a body forcing that is constant in time and varies sinusoidally in space. We find that linear stability analysis fails to predict the dynamical differences between low magnetic Reynolds number (Rm) flows and their higher Rm counterparts. We demonstrate two dynamical regimes, a low Rm regime and a filament regime in which the magnetic field is concentrated into a characteristic filament. We study how different forms of momentum transport (Reynolds vs Maxwell stresses) compare across parameter space and demonstrate differing trends between the two regimes.

1. INTRODUCTION

Shear flows are present in many astrophysical systems including stellar interiors (Miesch & Toomre 2009; Witzke, V. et al. 2015), relativistic jets found in active galactic nuclei (Alves et al. 2014), and accretion disks (Matsumoto & Tajima 1995). Due to the high Reynolds numbers of these systems, instabilities can arise at the shear flow boundary (Chandrasekhar 1961; Drazin 2002). These shear-flow instabilities drive turbulence, which increases the rate that momentum and heat are transported across the shear layer. The Kelvin-Helmoltz (KH) instability is a shear-driven instability that occurs when parallel flows of differing velocity have a shear strong enough to overcome stabilising effects such as buoyancy, viscosity, and magnetic tension (Chandrasekhar 1961; Drazin 2002). In stars, this has important effects for chemical mixing, and is a prime candidate for explaining some abundance anomalies (Brüggen & Hillebrandt 2001). Due to its relevance to astrophysical systems the KH instability has been extensively studied, and in idealised systems is well understood. However, the dynamics of this instability in the presence of a magnetic field are more complex and less

understood, despite magnetic fields being ubiquitous in the universe.

Currently, stellar models do not have efficient enough transport to match observations. In Red Giant Branch (RGB) stars at the luminosity bump, it is observed that lithium and CNO cycle by-products continue evolving with time, but stellar models do not predict this. This anomalous mixing is thought to occur due to thermohaline mixing, also known as fingering convection (Garraud 2018; Cantiello & Langer 2010). It was shown by Harrington & Garraud (2019) that adding a background magnetic field increases the efficiency of mixing enough to explain these observations. As the strength of the background magnetic field increases, the fingers become more coherent and elongated along the vertical direction and have a higher vertical velocity. This increase in the vertical velocities within the fingers causes a substantial increase in the vertical turbulent compositional fluxes. Prior work by Brown et al. (2013) found that, without magnetic fields, fingering convection cannot explain the anomalous mixing. Introducing magnetic fields to these systems leads to complex KH instabilities developing, and the parameter regime is relatively unexplored. Here,

we study the effect of strong resistive magnetic fields on KH instabilities in these regimes.

Magnetic fields that are aligned with the flow have a stabilising effect on KH instabilities due to the magnetic tension force (Chandrasekhar 1961), which acts as restoring force that straightens out bent magnetic field lines. An increased field strength reduces growth rate and can stabilise KH altogether. The stability threshold depends on the details of the system, but for ideal MHD roughly occurs when the Alfvén speed matches the change in flow velocity across the shear layer. Resistivity, however, can break the constraint of magnetic fields suppressing the instability. Resistivity breaks the frozen-in constraint, and reduces the bending of magnetic field lines by the flow, and thus lowers the magnetic tension. As you increase resistivity the field becomes less frozen in which means resistivity acts as a destabilising mechanism (Palotti et al. 2008) and can allow instabilities to grow even when ideal MHD predicts they should not.

To stabilise KH the field strength must exceed a certain threshold (Chandrasekhar 1961). Weaker magnetic fields are still unstable to KH, but have a reduced growth rate (Keppens et al. 1999). These fields can enhance the generation of small scale fluctuations, thus increasing mixing and momentum transfer across shear layers (Palotti et al. 2008; Fraser et al. 2021). The magnetic field is wound up until it reconnects, injecting energy into smaller scale eddies which, in turn, wind up the field until reconnection (Malagoli et al. 1996). This leads to a cascade of energy to smaller and smaller scales. The succession of intermittent reconnection events results in the perturbed magnetic energy to be dampened out (Palotti et al. 2008). This causes a rapid increase in shear layer width, thus enhancing mixing across the layer, driven by the small scale turbulence. This destruction of the large-scale eddies through cycles of windup and resistive decay changes when the resistivity is altered. The rate of resistive decay decreases with decreasing resistivity and thus momentum transport is increased (Palotti et al. 2008). The process is well understood for weak fields, however it is not clear the implication that strong-field resistive MHD has on such systems.

Many instabilities including the fingering instability, the Goldreich-Schubert-Fricke (GSF) instability, and the magnetorotational instability (MRI), drive sinusoidal shear flows that can become unstable to so-called “parasitic” instabilities. Rather than studying the developed shear flow on top of more complex physics like thermohaline mixing and GSF instabilities, we isolate these shear flows and look at the mixing and transport within

it. We explore how different forms of momentum transport compare in a strong-field resistive MHD regime, which has not been explored in previous work. We compare momentum transport across parameter space, determining how altering the strength of the background field and the level of resistivity affects the Reynolds and Maxwell stresses.

2. BACKGROUND AND METHODOLOGY

We use the pseudospectral code Dedalus (Burns et al. 2020) to study the evolution of a free shear layer in an incompressible fluid with finite viscosity and resistivity, governed by the magnetohydrodynamic (MHD) equations,

$$\rho_0 \left(\frac{\partial}{\partial t} + \mathbf{v} \cdot \nabla \right) \mathbf{v} = -\nabla p + \frac{1}{c} \mathbf{J} \times \mathbf{B} + \rho_0 \nu \nabla^2 \mathbf{v} + \mathbf{F}_0 \quad (2.1)$$

$$\frac{\partial}{\partial t} \mathbf{B} = \nabla \times (\mathbf{v} \times \mathbf{B}) + \eta \nabla^2 \mathbf{B} \quad (2.2)$$

$$\nabla \cdot \mathbf{v} = 0 \quad (2.3)$$

$$\nabla \cdot \mathbf{B} = 0, \quad (2.4)$$

where ρ_0 is the density, \mathbf{v} is the fluid velocity, p is the pressure, c is the speed of light, $\mathbf{J} = \nabla \times \mathbf{B}$ is the current density, \mathbf{B} is the magnetic field, ν is the viscosity, η is the magnetic diffusivity, and \mathbf{F}_0 represents external body forces. We consider periodic boundary conditions, and an initial, uniform magnetic field in the horizontal direction, $\mathbf{B}_0 = B_0 \hat{\mathbf{x}}$. Here, we consider a forcing of the form

$$\mathbf{F}_0 = F_0 \sin(k_0 z) \hat{\mathbf{x}}, \quad (2.5)$$

that maintains an unstable shear flow, without which the turbulence would decay. This is a time constant, spacial sinusoidal body forcing, and the shear flow it maintains is referred to as “Kolmogorov flow”.

The non-dimensionalisation used follows Cope et al. (2020) where the reference velocity, $[U]$, is constructed by assuming a dominant balance between $\mathbf{v} \cdot \nabla \mathbf{v}$ and the forcing term. Using k_0 as the reference length scale, the reference velocity is defined as,

$$[U] = \sqrt{\frac{F_0}{k_0}}. \quad (2.6)$$

In this non-dimensionalisation the flow amplitude is 1 in the turbulent state where forcing balances the inertial term. Conversely, in the laminar solution (the unstable equilibrium solution where there are no perturbations

and forcing purely balances dissipation, not inertia) has an amplitude of Re , not of 1.

Using equilibrium field strength B_0 as the reference magnetic field and the reference velocity defined above leads to the following non-dimensionalised equations,

$$\left(\frac{\partial}{\partial t} + \tilde{\mathbf{v}} \cdot \nabla\right) \tilde{\mathbf{v}} = -\nabla\tilde{P} + H_B \tilde{\mathbf{J}} \times \tilde{\mathbf{B}} + \frac{1}{\text{Re}} \nabla^2 \tilde{\mathbf{v}} + \sin(z) \hat{\mathbf{x}} \quad (2.7)$$

and

$$\frac{\partial}{\partial t} \tilde{\mathbf{B}} = \nabla \times (\tilde{\mathbf{v}} \times \tilde{\mathbf{B}}) + \frac{1}{\text{Rm}} \nabla^2 \tilde{\mathbf{B}}, \quad (2.8)$$

where non-dimensional fields are denoted with $\tilde{\cdot}$, and non-dimensionalization of coordinates \mathbf{x} and t is implied. Henceforth, the notation $\tilde{\cdot}$ is dropped for convenience. The strength of the background field H_B is controlled by the parameter

$$H_B = \frac{v_A^2}{[U]^2} \propto \frac{B_0^2}{F_0/k_0}. \quad (2.9)$$

where v_A is the Alfvén velocity. Thus, increasing the background field strength increases H_B and therefore increases the contribution of the Lorentz force in Eq. (2.7). For this system the ideal MHD threshold for stabilising KH is $H_B = 0.5$. The Reynolds number, Re , describes how turbulent or laminar the flow is and is defined as,

$$\text{Re} = \frac{[U]}{k_0 \nu} = \frac{\sqrt{F_0}}{k_0^{3/2} \nu}. \quad (2.10)$$

The magnetic Reynolds number, Rm , is defined as the ratio of the magnetic induction to magnetic diffusion,

$$\text{Rm} = \frac{[U]}{k_0 \eta} = \frac{\sqrt{F_0}}{k_0^{3/2} \eta}. \quad (2.11)$$

Since the magnetic Reynolds number alters the resistive MHD term in the induction Eq. (2.1) it thus alters the resistivity of the system: a higher Rm results in a lower resistivity. Re and Rm are related through the magnetic Prandtl number Pm which determines the ratio of the viscous diffusion rate to the magnetic diffusion rate,

$$\text{Pm} = \frac{\nu}{\eta}. \quad (2.12)$$

2.1. 2D case

In the 2D case the streamfunction ϕ and flux function ψ may be defined such that $\mathbf{v} = \hat{\mathbf{y}} \times \nabla \phi$ and $\mathbf{B} = \mathbf{B}_0 + \hat{\mathbf{y}} \times \nabla \psi$ (where $\mathbf{B}_0 = \hat{\mathbf{x}}$). This makes $\nabla^2 \phi$ the y component of vorticity, and $\nabla^2 \psi$ the y component of current density.

Then the equations become:

$$\begin{aligned} \frac{\partial}{\partial t} \nabla^2 \phi + \{\nabla^2 \phi, \phi\} = \\ H_B^2 (\{\nabla^2 \psi, \psi\} + \nabla^2 \partial_x \psi) + \frac{1}{\text{Re}} \nabla^4 \phi + \cos(z) \end{aligned} \quad (2.13)$$

$$\frac{\partial}{\partial t} \psi = \{\phi, \psi\} + \partial_x \phi + \frac{1}{\text{Rm}} \nabla^2 \psi \quad (2.14)$$

(where $\{f, g\} \equiv \partial_x f \partial_z g - \partial_z g \partial_x f$).

We consider an initial flow in the $\hat{\mathbf{x}}$ direction that varies in the $\hat{\mathbf{z}}$ direction. We solve these with an initially uniform magnetic field in the direction of the flow, $\mathbf{B} = B_0 \hat{\mathbf{x}}$. The control parameters H_B , Re , Pm , were altered, with values ranging from 0.1-3.0, 10-150, and 0.01 to 2 respectively. This results in a magnetic Reynolds number range from 0.01 to 200.

We use the pseudospectral code Dedalus (Burns et al. 2020) to study the evolution of the shear flow. We use Fourier spectral bases in both the x and z directions, with periodic boundary conditions on all sides. We use a box size of $8\pi \times 10\pi$, which is sufficient to capture multiple unstable Fourier modes, and a resolution of 128×256 .

The strong-field resistive regime of parameter space is relatively unexplored. In order to aid the exploration, linear stability diagrams were used, an example of which is shown in Figure 1. Figures 1a and 1b show the maximum growth rate for the unstable mode and the k_x value for which this occurs respectively as the Reynolds number and H_B are varied for $\text{Pm}=0.01$. Similarly Fig 1c and 1d also show this, but for a Pm equal to 0.5. These growth rates and k_x values correspond to perturbations about $U = \sin(z)$ and $B_0 = \hat{\mathbf{x}}$. The input parameters were chosen such that they fall in the regions of these graphs that have a large growth rate, which can be seen in Figure 2. Whilst the system is still unstable in the purple regions of the plots, the growth rates are small and the k_x for which they occur are also small. This means it requires a large box size in order to capture the unstable mode, which is more computationally difficult. These regions of parameter space will be explored in future work, but this project focuses on those parameters that fall within the larger growth rate regime.

At higher Reynolds number in Fig 2a and 2b the instability transitions to the low growth rate regime at $H_B = 0.5$. At lower Reynolds numbers however, the critical H_B for which this transition occurs is much larger. This due to the resistivity being able to break through the constraint and produce instabilities where

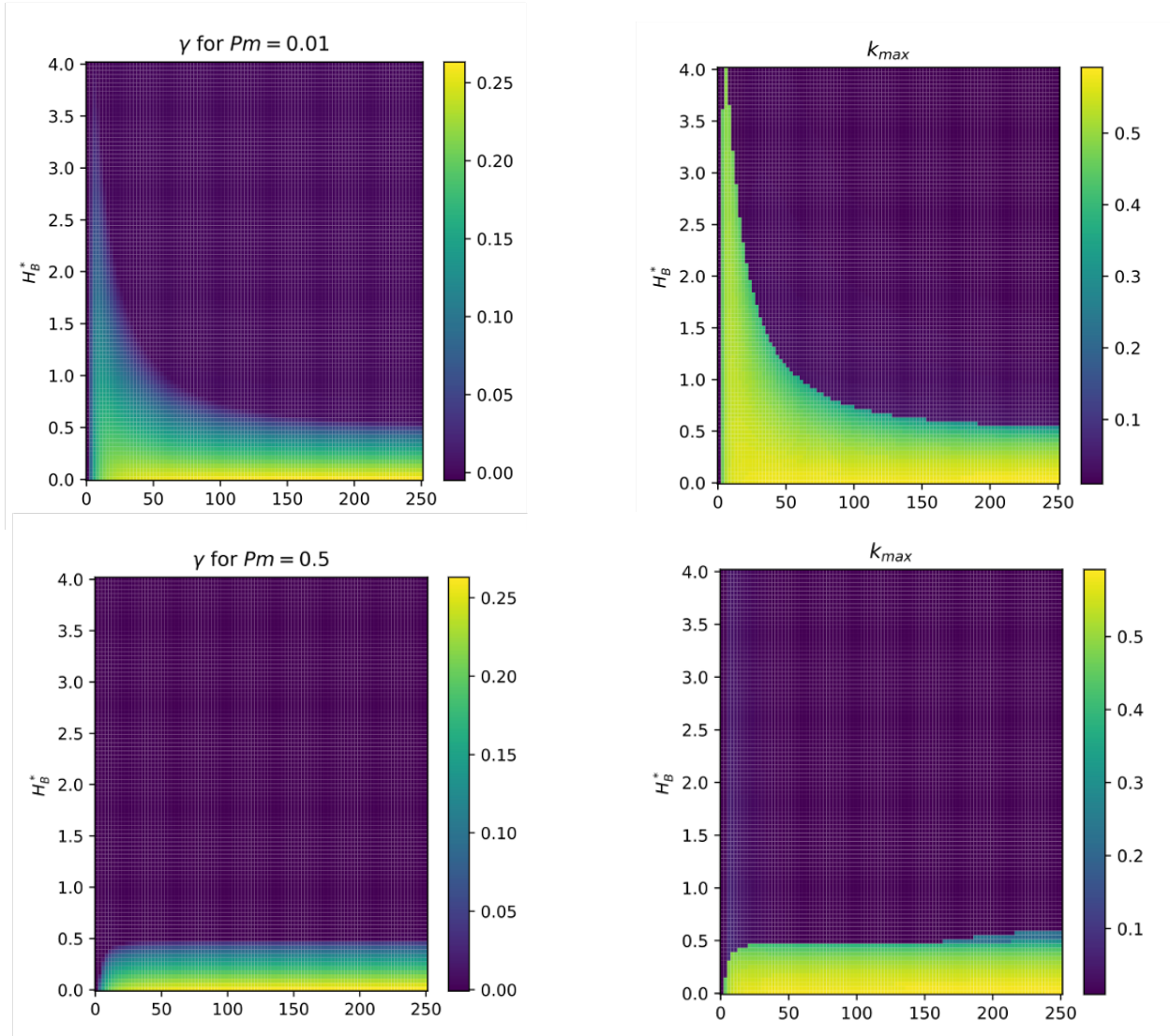


Figure 1: Results from linear stability analysis for two different magnetic Prandtl numbers $Pm=0.01$ (top) and $Pm=0.5$ (bottom) showing the maximum growth rate (left), and the k_x it occurs at (right). Note that the x -axis here is Reynolds number. For $Pm=0.01$, Rm can reach low enough values such that resistivity can break the constraint allowing relatively large growth rates at $H_B > 0.5$, whilst $Pm=0.5$ does not demonstrate this.

ideal MHD would not. If this were ideal MHD (i.e no resistivity) the peak at low Reynolds number would not occur. This can be seen in Fig 2c and 2d, where $Pm=0.5$ rather than $Pm=0.01$. Here the critical H_B remains at 0.5 or less regardless of the Reynolds number. A small deviation from this happens at high Re where there are some unstable modes at a relatively large k_x occurring above $H_B = 0.5$ (shown as a small bump starting at Re

≈ 160 in Fig 2d). This does not exist in ideal MHD and is something we will explore in future work.

In the chosen non-dimensionalisation, the resistive term in Eq 2.8 has a factor of $1/Rm$. This means increasing the magnetic Reynolds number decreases the effect of the resistivity and the system acts more like ideal MHD. Since $Pm=0.5$ in Fig 2c and 2d, the Reynolds number cannot get low enough such that the resistiv-

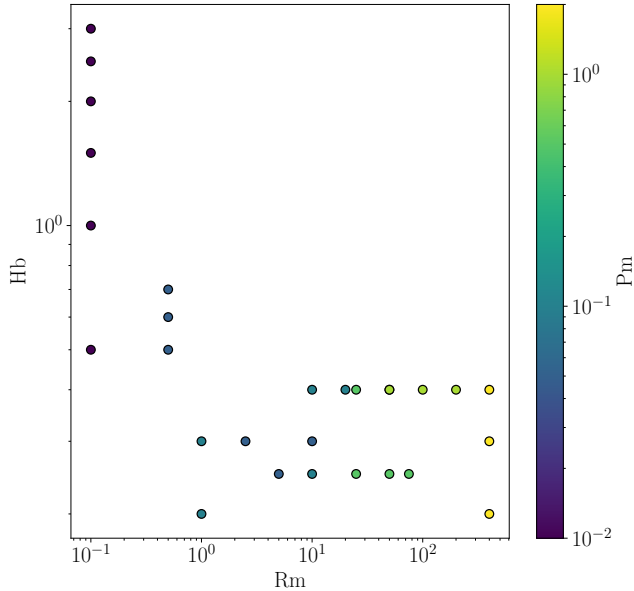


Figure 2: Input parameters for each simulation as a function of R_m and H_B with the colour scale denoting P_m . Note that higher values of H_B can be achieved for lower values of R_m due to resistivity breaking the instability constraint.

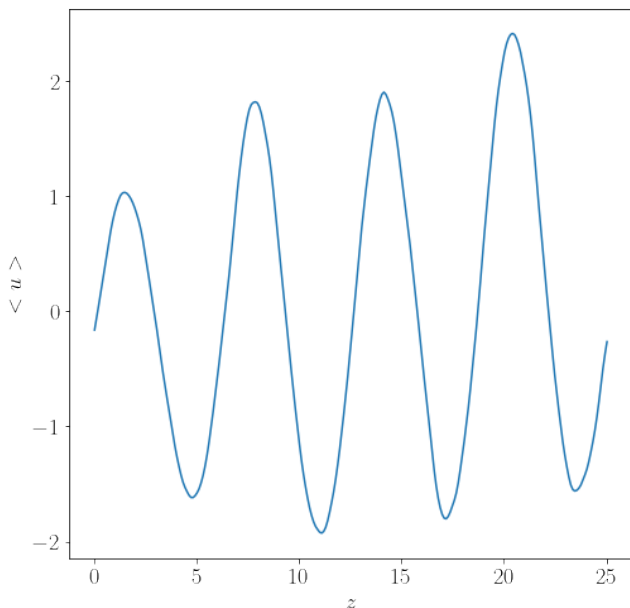


Figure 3: Horizontally averaged velocity profile for $P_m=0.5$, $H_B=0.2$, $Re=50$.

ity can break the instability constraint resulting in the critical H_B staying constant. This is why in Fig 1 the simulations ran at low R_m can have a large H_B whereas those at higher R_m stay below $H_B = 0.5$.

3. RESULTS AND DISCUSSION

3.1. Extracting true values of H_B and R_m

The dimensionless numbers H_B and R_m , Eq. (2.9) and Eq. (2.11), respectively, are defined in terms of a reference velocity. In the turbulent state, the flow speed defined in Eq. (2.6) is not the most relevant flow speed to use. The *rms* flow speed has contributions from mean flow and from fluctuations, so this is also not ideal. In order to extract the true flow speed we look at the horizontally averaged u profile for each simulation, an example of which is shown in Fig 3, which is near sinusoidal. We extract the sinusoidal component using a Fourier transform to use as the true reference flow speed. The true values of H_B and R_m are thus defined as,

$$H_B = \frac{H_B(\text{input})}{U_{\text{true}}^2} \quad \text{and} \quad R_m = R_m(\text{input}) \times U_{\text{true}}. \quad (3.1)$$

From this point onwards all H_B and R_m values quoted are the true values, and results are often reported in terms of the product $H_B R_m$, motivated by anticipated trends in the limit of low R_m (Davidson 2016, and P. Garaud, private communications).

3.2. Dynamical Regimes

When looking at the linear stability diagrams it is not obvious that the dynamics of these systems really change. Other than the peak at low R_m , there are not any major differences in growth rate or the k_x for which the unstable mode occurs. Fig 3 shows a snapshot of the non-linear dynamics for two very different areas of parameter space, with Fig 3a and 3c showing the magnitude of the magnetic field, and Fig 3b and 3d showing the corresponding streamfunction. This shows how much the dynamics vary over the parameter space. The top panel is in a low R_m regime, with $P_m 0.01$, $Re=10$, and $H_B = 1$ whereas the bottom panel is not with $P_m=0.5$, $Re=150$, and $H_B=0.25$. In the low R_m regime the magnetic field strength oscillates about 1 and has no defined features or dominant directions. In contrast, the magnetic field at higher R_m shows a strong filament of magnetic field just above the centre of the box. This filament moves slightly with the flow and is not disrupted for the duration of the simulation. It is robust to increasing box size, both in the x and z directions and occurs when $H_B R_m \geq 1$. This regime of parameter space is thus named the filament regime. Comparing the streamfunction snapshots, the low R_m simulation is less turbulent, with fewer eddies, which is most likely due to the large contrast in Reynolds number between the simulations. The striking difference in the dynamics of the two regimes indicates that non-linear simulations are

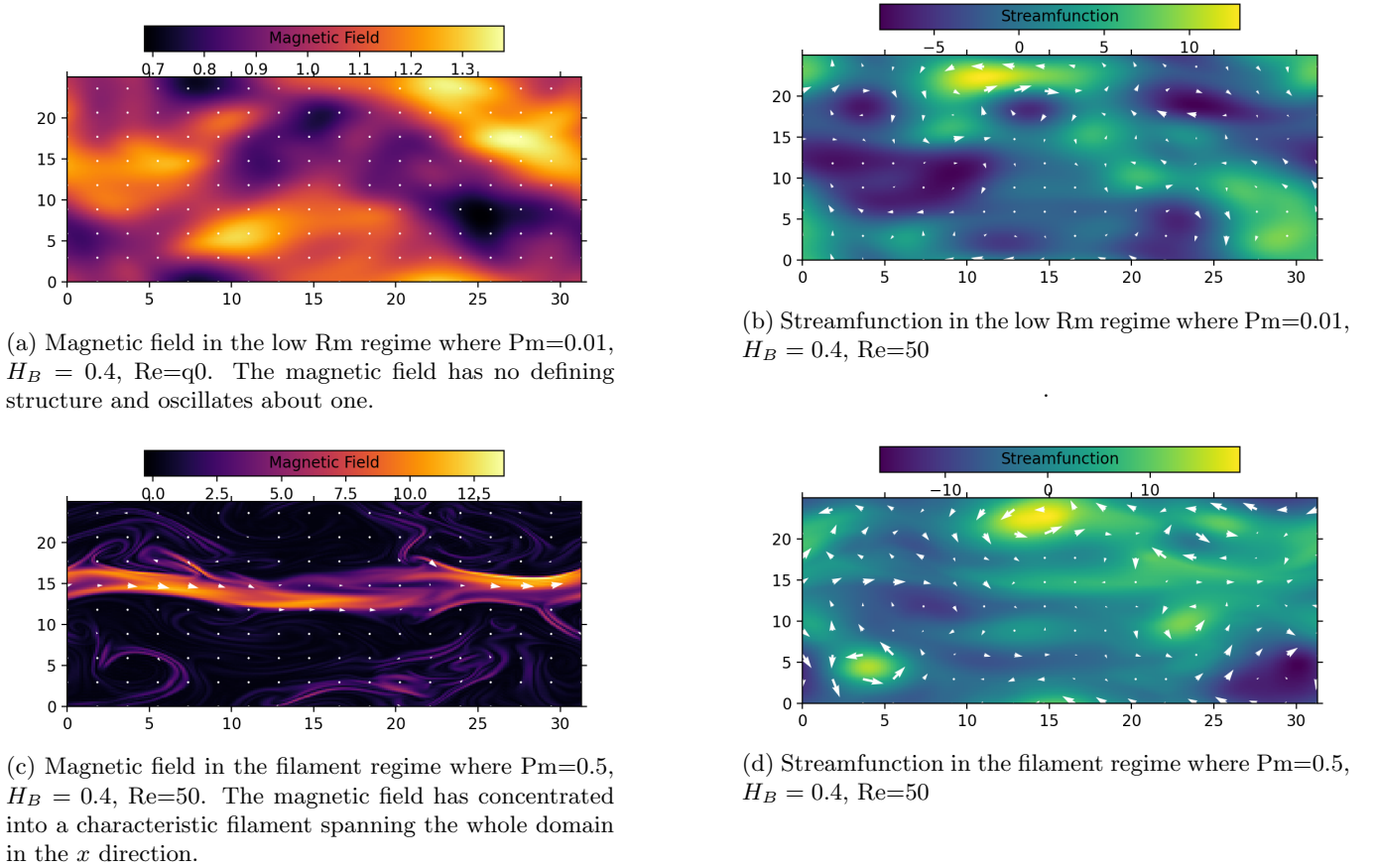


Figure 4: Snapshots of the magnetic field (left) and streamfunction (right) for two different regimes, the low Rm regime (top) and the filament regime (bottom)

required to understand these systems, as linear stability analysis fails to predict any major differences across parameter space.

Not only are the regimes visually different, but they also follow different trends in the kinetic and magnetic energies. Figure 5 shows how the kinetic energy scales with the output $H_B Rm$ in different regimes. The bottom left portion of the plot shows the low Rm regime, the centre shows a transition regime where the dynamics are more defined but do not show the characteristic filament, and the top right shows the filament regime. The simulations that fall into the low Rm regime have a kinetic energy that decreases with $H_B Rm$, whereas those that fall in the filament regime appear somewhat uncorrelated. It seems that through the transition regime, where the dynamics have begun to have more structure and the magnitude of the magnetic field is stronger but has not quite formed a filament, the kinetic energy increases with $H_B Rm$. Whilst the low Rm regime trend can be explained, it's not clear what the significance of

the trend, or lack thereof, is in the filament regime and thus more analysis is needed.

For the low Rm regime, the dependence of the kinetic energy on $H_B Rm$ can be explained by manipulating Eq. 2.7. By taking the limit where $Rm \ll 1$, a reduced version of the momentum equation (Eq. 2.7) can be derived (for the full derivation see Davidson (2016)),

$$\left(\frac{\partial}{\partial t} + \mathbf{v} \cdot \nabla\right) u = -\frac{\partial p}{\partial x} + \frac{1}{Re} \nabla^2 u + \sin(z), \quad (3.2)$$

$$\left(\frac{\partial}{\partial t} + \mathbf{v} \cdot \nabla\right) v = -\frac{\partial p}{\partial y} - H_B Rm v + \frac{1}{Re} \nabla^2 v, \quad (3.3)$$

and

$$\left(\frac{\partial}{\partial t} + \mathbf{v} \cdot \nabla\right) w = -\frac{\partial p}{\partial z} - H_B Rm w + \frac{1}{Re} \nabla^2 w, \quad (3.4)$$

where Eq. 3.2, Eq. 3.3, Eq. 3.4, are the x , y , and z components respectively. Comparing to Eq. 2.7, the Lorentz

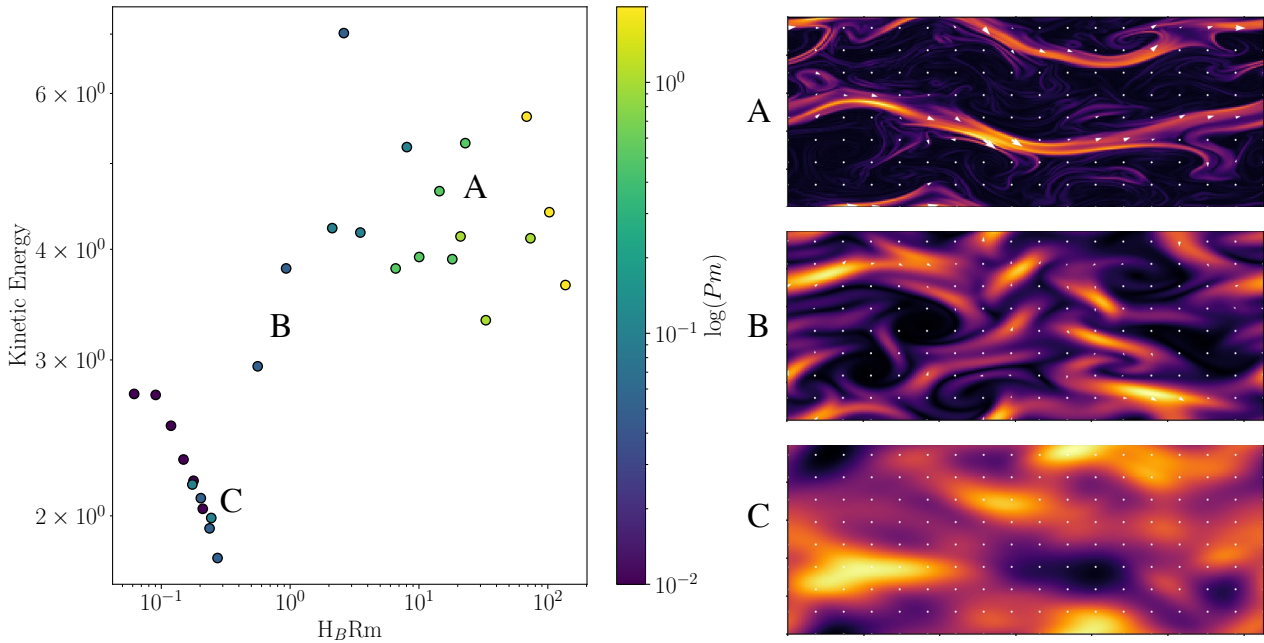


Figure 5: Plot showing kinetic energy trends with $H_B Rm$ in each regime. A) filament regime, B) Transition regime, C) Low Rm regime. In the Low Rm regime kinetic energy decreases with $H_B Rm$ due to drag term in Eq. 3.2-3.4.

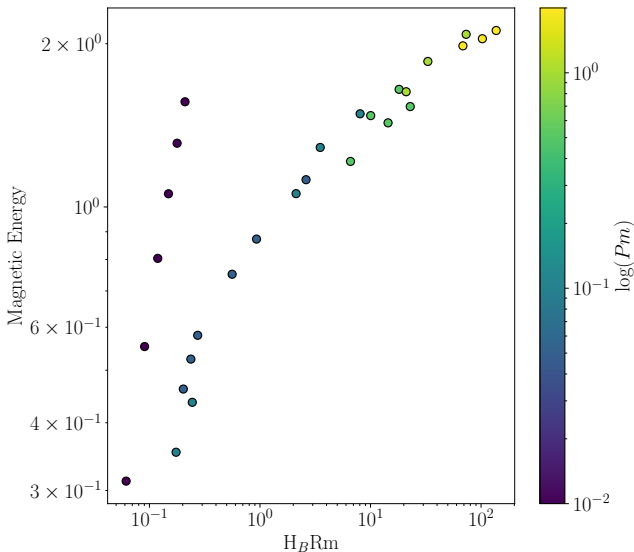


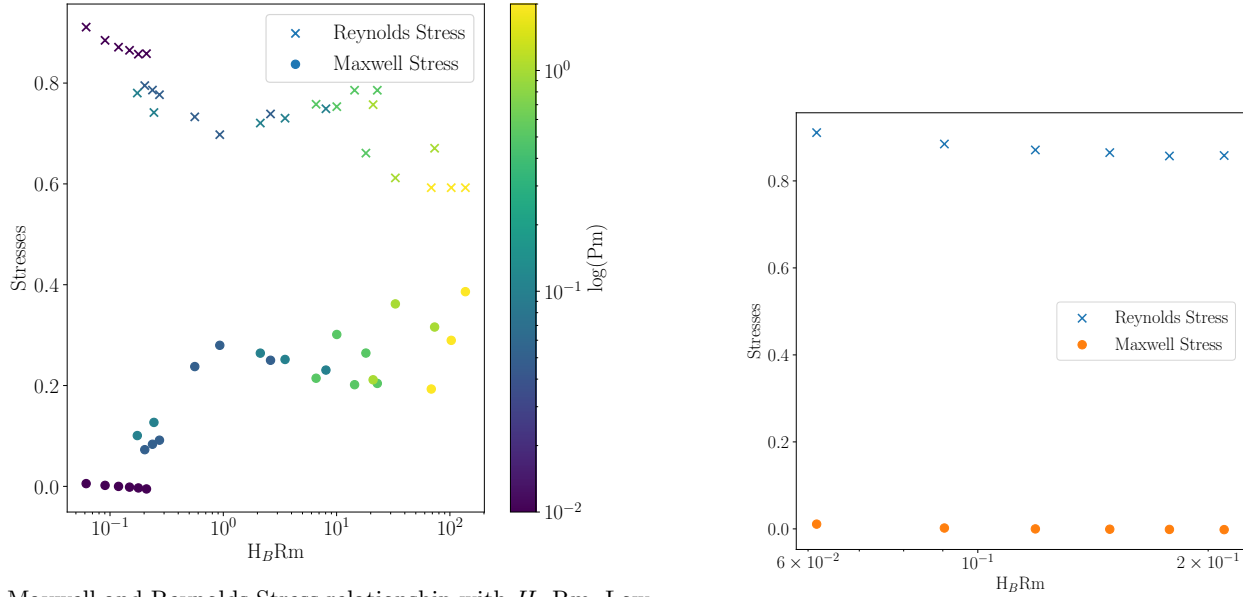
Figure 6: Magnetic energy trends with $H_B Rm$. Low Rm regime (purple) follows a steep increase with $H_B Rm$, whilst filament regime (blue-yellow) follows a flatter trend.

force $H_B \mathbf{J} \times \mathbf{B}$ becomes an anisotropic drag term with coefficient $H_B Rm$ that only acts in the y and z directions (just the z -direction for the 2D system). In this low Rm limit, increasing $H_B Rm$ increases the strength of this

drag term and thus reduces the amplitude of turbulent fluctuations. This brings the mean flow closer to its laminar solution, which has an amplitude of Re , in contrast with the turbulent solution, which has an amplitude of 1. Overall, the reduction in turbulent fluctuations has a larger effect on the total kinetic energy than the increased mean flow amplitude, and thus kinetic energy decreases with increased $H_B Rm$.

The magnetic energy follows a slightly different trend, which can be seen in Fig 6. In the low Rm regime the magnetic energy follows a much steeper trend with $H_B Rm$, compared to the filament regime which has a flatter dependency. Outside of the low Rm regime, these points follow trends that are consistent with previous work, in that magnetic energy scales with $H_B Rm$. Increasing Rm allows the field to cascade to smaller and smaller scales, thus there is more room to hold magnetic energy across different scales. Resistivity acts as a dissipation for magnetic energy. Increasing Rm decreases the resistivity, due to the $1/Rm$ dependence. The less resistivity the system has, the less the magnetic field is dissipated away thus resulting in an increase in magnetic energy as Rm increases.

For the Low Rm regime it is not as obvious why the magnetic energy follows this trend. In the reduced equa-



(a) Maxwell and Reynolds Stress relationship with $H_B Rm$, Low Rm regime in purple, whilst filament regime is in blue/yellow. (b) Low Rm regime only, demonstrating zero Maxwell stress

Figure 7: Maxwell and Reynolds Stresses across parameter space. Low Rm regime has Maxwell stress of zero since Lorentz term is not present in Eq. 3.2.

tions for $Rm \ll 1$ (Eq 3.1-3.3) there is no B term. The only magnetic term is $H_B Rm$ which acts as a factor on the velocities. This means the magnetic energy is not dynamically relevant quantity and does not affect the flow the way it does in for larger Rm .

3.3. Reynolds and Maxwell Stresses

In order to see how momentum transport varies across parameter space, the Reynolds, τ_u , and Maxwell, τ_b stresses were analysed in each regime. These stresses transport horizontal momentum vertically across a layer, due to shear forces, and are defined as,

$$\tau_u = - \left\langle \frac{\partial}{\partial x} \phi \frac{\partial}{\partial z} \phi \right\rangle_x, \quad (3.5)$$

$$\tau_b = H_B^2 \left\langle \frac{\partial}{\partial x} \psi \frac{\partial}{\partial z} \psi \right\rangle_x, \quad (3.6)$$

where $\langle \cdot \rangle_x$ denotes a horizontal average.

The Reynolds stress transports momentum due to turbulence. When a flow is turbulent rather than laminar, turbulent motions drive additional momentum fluxes. A more turbulent flow has a higher Reynolds stress and has a net momentum transfer because of the increased mixing of the fluid elements. When magnetic fields are included, the Lorentz force also produces a shear force and hence can transport momentum, defined by the Maxwell stress. The two stresses evolve the mean flow $\langle U \rangle_x$ ac-

ording to,

$$\frac{\partial}{\partial t} \langle U \rangle_x = \frac{\partial}{\partial z} (\tau_u + \tau_b) + \sin z, \quad (3.7)$$

where viscosity has been neglected and the $\cos z$ is the forcing term.

Figure 7a shows that in the low Rm regime, the simulations have effectively zero Maxwell stress across the layer. Outside of that regime in the filament regime, the Maxwell stress increases with $H_B Rm$. This is due to the same reason that the magnetic energy increases with $H_B Rm$, as the field strength increases, so does the Lorentz force, thus the shear force it provides gets larger resulting in more momentum transport. Also, increasing Rm decreases the effect of resistivity which in turn results in an increased Maxwell stress across the layer.

Figure 7b shows the Reynolds and Maxwell stresses in just the low Rm regime. Here it is quite clear that the Maxwell stress in this regime is zero. This can be explained by again looking at the low Rm equations (Eq. 3.2 - Eq. 3.4). The x equation (Eq. 3.2) has no magnetic term, the Lorentz term only shows up in the y (Eq. 3.3) and z (Eq. 3.4) equations. The Maxwell stress term, by definition, appears when horizontally averaging these equations. Since there is no magnetic term in the x equation, there cannot be any Maxwell stress.

Figure 8 shows the Maxwell stress profile (left) in the filament regime, for two different Reynolds numbers

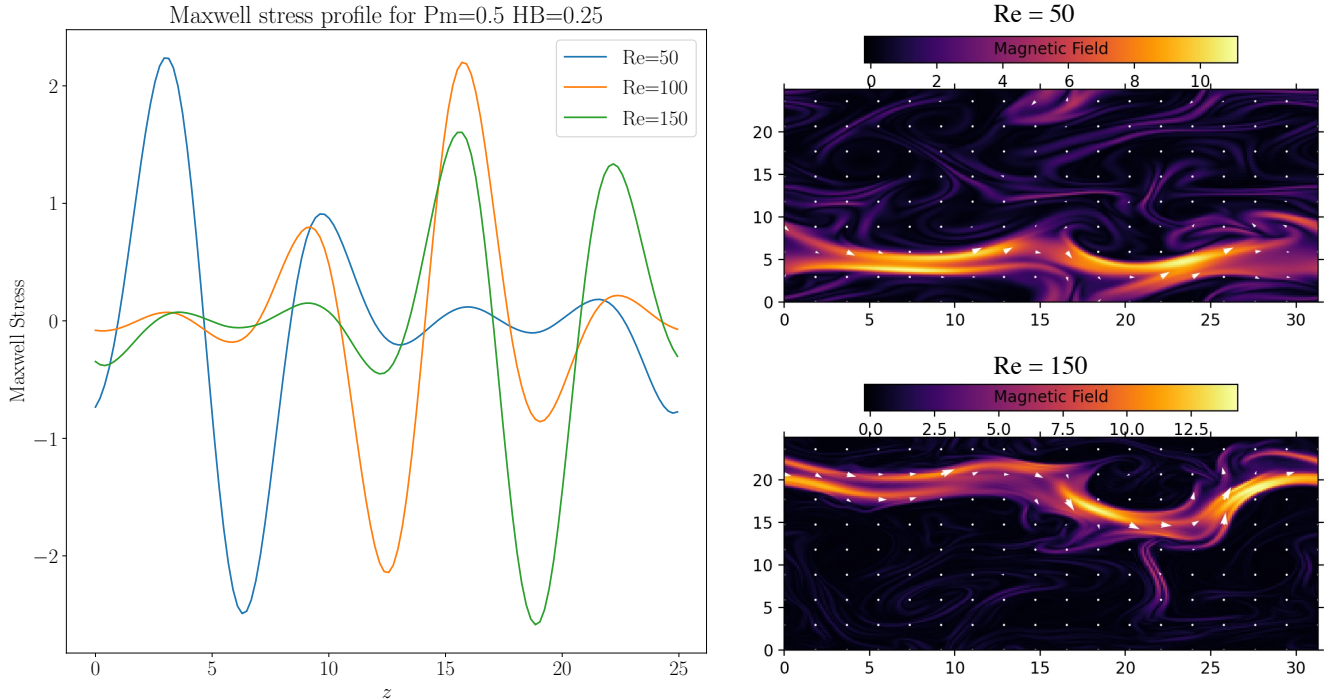


Figure 8: Maxwell stress profile (left) and snapshots of filament (right) for different Reynolds numbers $Re=50$ (blue), $Re=100$ (orange), $Re=150$ (green). Location of filament corresponds to large peaks in the Maxwell stress.

$Re=50$ (blue), $Re=100$ (orange), and $Re=150$ (green) alongside a snapshot of magnetic field for $Re=50$ (top) and $Re=150$ (bottom). For a $Re=50$, the peaks of the Maxwell stress profile are large at the bottom of the domain ($z=0-10$) whilst peaks are close to zero at the top of the domain ($z=15-25$). Comparing that to the image of the magnetic field, the location of the large peaks corresponds to the location of the filament in the domain. Conversely, for $Re=150$ (green), the large peaks occur at the top of the domain which is, again, where the filament is located. Maxwell stress increases with increasing magnetic field, and since the filament is a region of concentrated magnetic field, it has the strongest Maxwell stress. This result is very qualitative and in future work this will be explored further.

4. CONCLUSIONS & FUTURE WORK

Here we have presented a systemic parameter study of a two-dimensional MHD unstable shear flow and its evolution. We have found that linear stability analysis fails to predict the dynamical differences across parameter space, and that non-linear simulations are required for these simulations. Furthermore, we have identified two regimes in which the dynamics and trends for kinetic and magnetic energy along with values for the Maxwell and Reynolds stresses differ drastically:

1. The low Rm regime, which occurs for $H_B Rm < 1$, where magnetic field strength oscillates about one and has no defined features or dominant directions. The kinetic energy decreases with the parameter $H_B Rm$, whilst the magnetic energy increases. Maxwell stresses in this regime were found to be 0.
2. The filament regime, which occurs for $H_B Rm \geq 1$, where magnetic field demonstrates a characteristic filaments spanning across the whole domain in the x direction. The kinetic energy follows no specific trend with $H_B Rm$. The Maxwell and Reynolds stress sum to one in this regime.

Whilst this study shows a stark difference between the two regimes, the results presented here are mainly qualitative. Future work will analyse these trends further in order to quantify these results. The filament regime is very interesting and so we will repeat this work in three-dimensions to see if similar trends occur. We will also conduct a deeper exploration of parameter space where growth rates are much smaller but still unstable.

ACKNOWLEDGEMENTS

We would like to thank Pascale Garaud for helpful comments on this work, and Keaton Burns for assistance

with optimizing Dedalus on the computing resources used. We would also like to thank the Kavli Program and its organisers for funding and supporting this work, as well as offering helpful lectures, seminars, and a nice virtual workspace. We acknowledge use of the lux super-

computer at UC Santa Cruz, funded by NSF MRI grant AST 1828315. This work used the Extreme Science and Engineering Discovery Environment (XSEDE) Expanse supercomputer at the San Diego Supercomputer Center through allocation TG-PHY210050.

REFERENCES

- Alves, E. P., Grismayer, T., Fonseca, R. A., & Silva, L. O. 2014, *New Journal of Physics*, 16, 035007, doi: [10.1088/1367-2630/16/3/035007](https://doi.org/10.1088/1367-2630/16/3/035007)
- Brown, J. M., Garaud, P., & Stellmach, S. 2013, 768, 34, doi: [10.1088/0004-637x/768/1/34](https://doi.org/10.1088/0004-637x/768/1/34)
- Brüggen, M., & Hillebrandt, W. 2001, *Monthly Notices of the Royal Astronomical Society*, 320, 73, doi: [10.1046/j.1365-8711.2001.03951.x](https://doi.org/10.1046/j.1365-8711.2001.03951.x)
- Burns, K. J., Vasil, G. M., Oishi, J. S., Lecoanet, D., & Brown, B. P. 2020, *Physical Review Research*, 2, doi: [10.1103/physrevresearch.2.023068](https://doi.org/10.1103/physrevresearch.2.023068)
- Cantiello, M., & Langer, N. 2010, *Astronomy & Astrophysics*, 521, A9, doi: [10.1051/0004-6361/201014305](https://doi.org/10.1051/0004-6361/201014305)
- Chandrasekhar, S. 1961, *Hydrodynamic and hydromagnetic stability* (Clarendon Press)
- Cope, L., Garaud, P., & Caulfield, C. P. 2020, *Journal of Fluid Mechanics*, 903, A1, doi: [10.1017/jfm.2020.600](https://doi.org/10.1017/jfm.2020.600)
- Davidson, P. A. 2016, *Introduction to Magnetohydrodynamics*, 2nd edn., *Cambridge Texts in Applied Mathematics* (Cambridge University Press), doi: [10.1017/9781316672853](https://doi.org/10.1017/9781316672853)
- Drazin, P. G. 2002, *Introduction to Hydrodynamic Stability*, *Cambridge Texts in Applied Mathematics* (Cambridge University Press), doi: [10.1017/CBO9780511809064](https://doi.org/10.1017/CBO9780511809064)
- Fraser, A. E., Terry, P. W., Zweibel, E. G., Pueschel, M. J., & Schroeder, J. M. 2021, *Physics of Plasmas*, 28, 022309, doi: [10.1063/5.0034575](https://doi.org/10.1063/5.0034575)
- Garaud, P. 2018, *Annual Review of Fluid Mechanics*, 50, 275, doi: [10.1146/annurev-fluid-122316-045234](https://doi.org/10.1146/annurev-fluid-122316-045234)
- Harrington, P., & Garaud, P. 2019, *The Astrophysical Journal*, 870, L5, doi: [10.3847/2041-8213/aaf812](https://doi.org/10.3847/2041-8213/aaf812)
- Keppens, R., TÓTH, G., WESTERMANN, R. H. J., & GOEDBLOED, J. P. 1999, *Journal of Plasma Physics*, 61, 1–19, doi: [10.1017/S0022377898007223](https://doi.org/10.1017/S0022377898007223)
- Malagoli, A., Bodo, G., & Rosner, R. 1996, *ApJ*, 456, 708, doi: [10.1086/176691](https://doi.org/10.1086/176691)
- Matsumoto, R., & Tajima, T. 1995, doi: [10.2172/10120439](https://doi.org/10.2172/10120439)
- Miesch, M. S., & Toomre, J. 2009, *Annual Review of Fluid Mechanics*, 41, 317, doi: [10.1146/annurev.fluid.010908.165215](https://doi.org/10.1146/annurev.fluid.010908.165215)
- Palotti, M. L., Heitsch, F., Zweibel, E. G., & Huang, Y.-M. 2008, *The Astrophysical Journal*, 678, 234, doi: [10.1086/529066](https://doi.org/10.1086/529066)
- Witzke, V., Silvers, L. J., & Favier, B. 2015, *A&A*, 577, A76, doi: [10.1051/0004-6361/201425285](https://doi.org/10.1051/0004-6361/201425285)